Pergamon

Planet. Space Sci., Vol. 43, No. 8, pp. 941–951, 1995

0032–0633/95 $9.50+0.00

0032–0633(94)00232–0

Reduction of *Galileo* and *Ulysses* dust data

E. Grün, M. Baguhl, D. P. Hamilton, J. Kissel, D. Linkert, G. Linkert and R. Riemann

Max-Planck-Institut für Kernphysik, 69029 Heidelberg, Germany

Received 14 September 1994; accepted 7 November 1994

Abstract. The reduction procedures which are applied to raw data from the *Galileo* and *Ulysses* Dust Detectors are described in order to obtain physical parameters (mass and velocity) for the recorded dust impacts. Both detectors are impact ionization detectors which measure the charge released from an impact onto a solid target. From the rise times of the signals, impact speeds from 2 to 70 km s^{-1} can be derived with an accuracy of about a factor 2. Electronic impact charges are measured from 10^{-14} to 10^{-8} C, which refer to a speed dependent mass range (e.g. 4×10^{-15}–4×10^{-9} g at 20 km s^{-1} impact speed). Larger particles are recorded with saturated signals. Data processing performed both on board the spacecraft and on the ground is described. The processing allows dust impacts to be identified and separated from noise events. Supplementary information, such as impact time and sensor pointing at the time of impact, is also provided.

Introduction

The *Galileo* and *Ulysses* Dust Detectors are both highly sensitive impact ionization detectors which detect the clouds of electrons and ions released during a hypervelocity impact onto a solid target. This effect was predicted theoretically by Raizer (1960), and was first verified experimentally by Friichtenicht and Slattery (1963). With the help of dust accelerators (for a review see Fechtig *et al.* (1978)), detailed studies of impact ionization were performed over the past 30 years which led to the development of sophisticated dust detectors. Impact ionization studies on a number of projectile and target material combinations have been carried out by Auer and Sitte (1968), Dalmann *et al.* (1976), Grün (1984), Kissel and Krueger (1987), Timmermann and Grün (1991) and others. Calibration tests of impact ionization detectors flown on various spacecraft have been described: *Pioneer* 8 and 9 (Grün *et al.*, 1973), *HEOS* and *Helios* (Dietzel *et al.*, 1973), *Giotto-PIA* (Kissel, 1986; Kissel and Krueger, 1987), *Giotto-DIDSY-IPM* (Göller *et al.*, 1986), *MUSES* (Iglseder and Igenbergs, 1987), and *Galileo* and *Ulysses* (Göller and Grün, 1989).

We use the results of the above studies, especially the last, to reduce raw *Galileo* and *Ulysses* data. In this paper, we describe how the raw data received from the *Galileo* and *Ulysses* Dust Detectors are reduced to physical parameters (mass and velocity) for the recorded dust impacts. The process can be divided into two steps: first, the data are reduced electronically (i.e. data numbers are converted to impact parameters such as electric charge and rise-time) after which they are interpreted physically (i.e. measured impact parameters are converted to the mass and velocity of the dust particle). We describe the data processing, both on board and on the ground, which enables reliable impact identification and provides supplementary information such as impact time and sensor pointing at the time of impact.

The data reduction scheme which is currently employed is mainly based on earlier impact tests with flight and spare instruments at the Heidelberg dust accelerator (e.g. Göller and Grün, 1989). We will continue to use this calibration until new information becomes available. New information may come from further impact tests with different projectile parameters (materials, masses, and speeds) or from astrophysical considerations such as a detailed comparison of results from the *Galileo* and *Ulysses* dust instruments. Separate dust populations (e.g. interplanetary, interstellar, and jovian dust) have particular characteristics (materials, masses, and velocities) which are observed by the two instruments under different conditions (especially different impact speeds). These differences should show up in the two data sets given sufficient statistical accuracy, thereby providing a possible means to check and perhaps improve the current calibrations.

In two companion papers, both the raw and reduced data are given for the first 3 years of *Galileo*'s orbital tour (Grün *et al.*, 1995a, henceforth Paper II) and for the first

Correspondence to: E. Grün

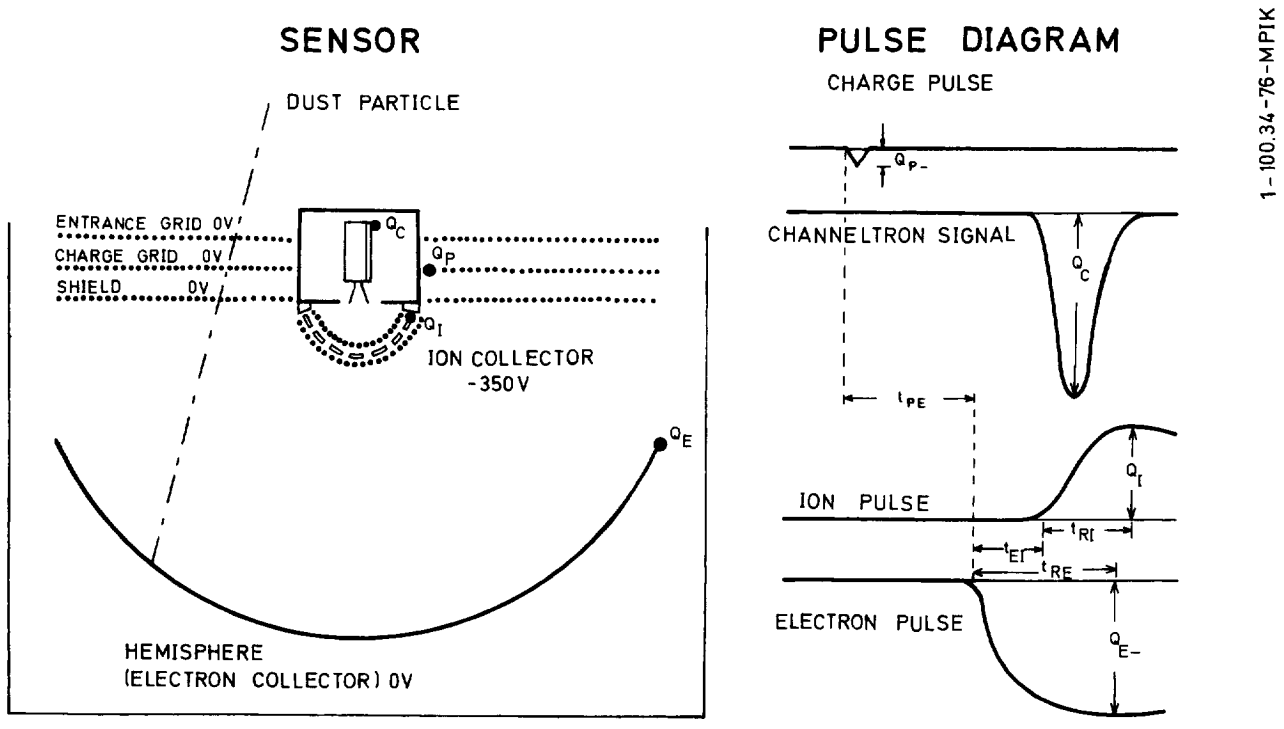

Fig. 1. Sensor configuration (schematic) and measured signals (pulse amplitudes Q_P, Q_C, Q_I, Q_E and times t_{PE}, t_{EI}, t_I, t_E) upon impact of a positively charged dust particle

2 years of *Ulysses*' journey (Grün *et al.*, 1995b, Paper III). The information presented in these three papers is equivalent to data which we are submitting to the various data archiving centers (Planetary Data System, NSSDC, *Ulysses* Data Center, etc.).

Instrument characteristics

Both the *Galileo* and the *Ulysses* Dust Detectors have been described previously (Grün *et al.*, 1992a, b) in reasonable detail. Therefore, only the basic features of the instruments are described here together with quantitative information about the data reduction process. Both instruments detect individual dust particles which strike the sensor's target by measuring the total number of ions and electrons released upon impact as well as the rise times of the associated charge pulses. From these data, the dust particle's mass, impact speed, electric charge, and impact direction are determined. The two instruments are of nearly identical design and consist of impact ionization sensors and appropriate electronics.

The measuring principle of the *Ulysses* sensor is illustrated in Fig. 1. If the magnitude of the electric charge is large enough, dust particles entering the sensor may be detected before impact by the charge Q_P that they induce on the charge grid while flying between the entrance and shield grids (Fig. 1). All suitably massive dust particles—charged or uncharged—are detected by the cloud of ions and electrons they produce during the impact on the hemispherical target. After separation in the electric field, ions and electrons are collected by separate electrodes. Charge sensitive amplifiers connected to these electrodes deliver two nearly coincident pulses of opposite polarity, Q_E and Q_I. In order to cover a wide dynamic range of 10^6, the signals are amplified by three parallel amplifier chains, each covering a dynamic range of about 100. The rise times of these pulses are also measured. Göller and Grün (1989) have shown that rise times are independent of the particle mass, and decrease with increasing particle speed. From the two pulse heights and the rise times, the mass and impact speed of the dust particle are derived by using empirical relations between these quantities established during calibration of the instruments. A third independent impact signal originates from the part of the positive ion cloud that is detected by the channeltron. This signal Q_C is an additional parameter for the identification of dust impacts. The thresholds and the dynamic ranges of the different signals measured upon impact are given in Table 1. Coincidences between various impact signals and status information (see Table 2) are also recorded for each event. The value of the spacecraft clock count and the spacecraft orientation at the time of the impact are also needed to determine the impact time and spacecraft attitude.

A measurement cycle can be initiated if one or more of the signals Q_E, Q_I or Q_C exceeds its threshold. Ground command determines which of the three signals actually initiates a measurement cycle and this information is recorded for each measurement by the status word EVD. The encoding of EVD is shown in Table 3. During normal operation, an event is initiated by signals Q_I or Q_C (EVD = 1). This selection was made because of the large noise rate for the electron signal Q_E.

All signal amplitudes and event times are digitized. Table 4 shows the charge levels of the different digitization steps for the four impact charge pulses. Tables 4a and b give the values for the *Galileo* Dust Detector and Tables 4c and d give the values for the *Ulysses* detector. Forty-

Table 1. Signals measured upon impact of a dust particle onto the sensor and related particle parameters

Signal/data names	Measured quantity	Range	Number of logarithmic steps	Related particle parameters
Q_E/EA	negative charge generated upon impact (electrons)	10^{-14}–10^{-8} C	48	mass, speed
Q_I/IA	positive charge generated upon impact (ions)	10^{-14} 10^{-8} C	48	mass, speed
Q_C/CA	positive charge generated upon impact (partially)	10^{-13}–10^{-9} C (channeltron output)	48	impact identification
Q_P/PA	induced charge positive	10^{-14}–10^{-12}	16	electrical
	induced charge negative	10^{-14}–10^{-10} C	32	charge
t_E/ET	rise-time of negative charge	10–100 μs	16	speed
t_I/IT	rise-time of positive charge	10–100 μs	16	speed
t_{EI}/EIT	time between negative and positive charge signals	−5 to 44 μs	16	impact identification
t_{PE}/PET	time between induced and negative charge signals	1–400 μs	32	speed

Table 2. Supplementary data channels of the *Galileo* and *Ulysses* Dust Detectors

Name	Bits	Description
CCP	2	Channeltron (Q_C) threshold setting
CLN	2	Class number of current event
CN	4	Channeltron noise counter
ECP	2	Negative charge (Q_E) threshold setting
EIC	1	Coincidence between negative and positive charge signals: if both pulses exceed the thresholds within 200 ns
EN	4	Target noise counter
EVD	3	Event definition status; actual setting for the initiation of data acquisition by one or more impact signals
HVC	8	Channeltron high voltage, range 0–2500 V commandable in 15 HV steps
ICC	1	Coincidence between ion and channeltron signals: if both pulses exceed their thresholds within 20 μs
ICP	2	Ion charge (Q_I) threshold setting
IN	4	Ion noise counter
PCP	2	Induced charge (Q_P) threshold setting
PN	4	Induced charge noise counter
SEC	8	Spacecraft sector (spin position angle) at time of event
TIME	8	Spacecraft clock count at time of event

Table 3. Event definition, EVD. The measuring channels which initiate a measuring cycle are indicated by an x

EVD	Q_I	Q_E	Q_C
0	x	x	x
1	x		x
2		x	x
3			x
4	x	x	
5	x		
6		x	

five approximately logarithmic steps are used to cover six orders of magnitude of the positive (Q_I) and negative (Q_E) impact charges. Eight digitization steps cover about one decade in charge and steps 32–47 are not used. Apparent gaps in the otherwise uniform amplitude sequences occur at steps 16 and 48. These are caused by transitions between different amplifiers.

The channeltron output charge Q_C is measured over a dynamic range of 10^4 in only 32 logarithmic steps. The charge at the channeltron output depends on the channeltron's amplification, one measure of which is the ratio between the channeltron output charge Q_C and the ion

Table 4a. Digitization steps (IA, EA, CA, PA) of signal amplitudes for the lower four decades of charge measurements Q_I, Q_E, Q_C, Q_P, for the *Galileo* Dust Detector. The indicated charge values correspond to the logarithmic mean of the lower and upper threshold values of the respective signal amplitude—unless upper and lower limits are explicitly given. The threshold levels have been electronically determined with pulses of 20 and 2 μs rise-times for impact charges Q_I, Q_E, Q_C and induced charge Q_P, respectively

IA	Q_I pos. (C)	EA	Q_E neg. (C)	CA	Q_C neg. (C)	PA	Q_P neg. (C)
0	$<1.0\times10^{-14}$	0	$<9.8\times10^{-15}$	0	$<1.0\times10^{-13}$	0	$<1.8\times10^{-14}$
1	1.23×10^{-14}	1	1.22×10^{-14}	1	1.41×10^{-13}	1	2.45×10^{-14}
2	1.73×10^{-14}	2	1.73×10^{-14}	2	2.28×10^{-13}	2	3.46×10^{-14}
3	2.43×10^{-14}	3	2.37×10^{-14}	3	2.88×10^{-13}	3	4.47×10^{-14}
4	3.46×10^{-14}	4	3.13×10^{-14}	4	3.75×10^{-13}	4	5.48×10^{-14}
5	4.47×10^{-14}	5	4.18×10^{-14}	5	5.14×10^{-13}	5	6.71×10^{-14}
6	6.33×10^{-14}	6	6.12×10^{-14}	6	6.93×10^{-13}	6	8.22×10^{-14}
7	9.22×10^{-14}	7	8.66×10^{-14}	7	8.94×10^{-13}	7	1.02×10^{-13}
8	1.23×10^{-13}	8	1.18×10^{-13}	8	1.18×10^{-12}	8	1.17×10^{-13}
9	1.73×10^{-13}	9	1.65×10^{-13}	9	1.59×10^{-12}	9	1.55×10^{-13}
10	2.37×10^{-13}	10	2.30×10^{-13}	10	2.12×10^{-12}	10	2.37×10^{-13}
11	3.26×10^{-13}	11	3.12×10^{-13}	11	2.83×10^{-12}	11	3.13×10^{-13}
12	4.57×10^{-13}	12	4.33×10^{-13}	12	3.80×10^{-12}	12	4.10×10^{-13}
13	6.42×10^{-13}	13	6.03×10^{-13}	13	5.20×10^{-12}	13	5.37×10^{-13}
14	8.87×10^{-13}	14	8.44×10^{-13}	14	6.93×10^{-12}	14	6.93×10^{-13}
15	1.12×10^{-12}	15	1.05×10^{-12}	15	8.94×10^{-12}	15	8.94×10^{-13}
16	1.12×10^{-12}	16	1.05×10^{-12}	16	8.94×10^{-12}	16	8.94×10^{-13}
17	1.47×10^{-12}	17	1.27×10^{-12}	17	1.18×10^{-11}	17	1.45×10^{-12}
18	1.99×10^{-12}	18	1.50×10^{-12}	18	1.72×10^{-11}	18	2.51×10^{-12}
19	2.57×10^{-12}	19	1.79×10^{-12}	19	2.51×10^{-11}	19	3.33×10^{-12}
20	3.10×10^{-12}	20	2.53×10^{-12}	20	3.46×10^{-11}	20	4.30×10^{-12}
21	4.00×10^{-12}	21	3.67×10^{-12}	21	4.56×10^{-11}	21	5.66×10^{-12}
22	6.12×10^{-12}	22	5.02×10^{-12}	22	5.95×10^{-11}	22	7.80×10^{-12}
23	8.66×10^{-12}	23	7.14×10^{-12}	23	7.82×10^{-11}	23	1.11×10^{-11}
24	1.18×10^{-11}	24	1.01×10^{-11}	24	1.06×10^{-10}	24	1.51×10^{-11}
25	1.59×10^{-11}	25	1.43×10^{-11}	25	1.48×10^{-10}	25	2.09×10^{-11}
26	2.16×10^{-11}	26	1.98×10^{-11}	26	2.01×10^{-10}	26	2.87×10^{-11}
27	2.93×10^{-11}	27	2.71×10^{-11}	27	2.78×10^{-10}	27	3.85×10^{-11}
28	3.81×10^{-11}	28	3.75×10^{-11}	28	3.88×10^{-10}	28	5.22×10^{-11}
29	5.35×10^{-11}	29	4.96×10^{-11}	29	5.73×10^{-10}	29	7.17×10^{-11}
30	7.60×10^{-11}	30	6.35×10^{-11}	30	1.34×10^{-9}	30	1.10×10^{-10}
31	9.67×10^{-11}	31	8.49×10^{-11}	31	$>2.45\times10^{-9}$	31	$>1.20\times10^{-10}$

Table 4b. Digitization steps (IA, EA, PA) of signal amplitudes Q_I, Q_E, Q_P for the upper two decades of Q_I and Q_E and positive charges Q_P—for the *Galileo* Dust Detector. For further explanations see Table 4a

IA	Q_I pos. (C)	EA	Q_E neg. (C)	PA	Q_P pos. (C)
48	9.67×10^{-11}	48	8.49×10^{-11}	32	$<9.2\times10^{-15}$
49	1.48×10^{-10}	49	1.73×10^{-10}	33	1.23×10^{-14}
50	2.53×10^{-10}	50	3.46×10^{-10}	34	1.73×10^{-14}
51	3.75×10^{-10}	51	4.20×10^{-10}	35	2.24×10^{-14}
52	4.83×10^{-10}	52	4.96×10^{-10}	36	3.16×10^{-14}
53	6.31×10^{-10}	53	6.48×10^{-10}	37	4.90×10^{-14}
54	8.66×10^{-10}	54	8.66×10^{-10}	38	6.93×10^{-14}
55	1.19×10^{-9}	55	1.24×10^{-9}	39	9.38×10^{-14}
56	1.76×10^{-9}	56	1.84×10^{-9}	40	1.28×10^{-13}
57	2.69×10^{-9}	57	2.78×10^{-9}	41	1.77×10^{-13}
58	3.41×10^{-9}	58	4.66×10^{-9}	42	2.51×10^{-13}
59	1.08×10^{-8}	59	1.16×10^{-8}	43	3.46×10^{-13}
60	$>2.2\times10^{-8}$	60	$>2.2\times10^{-8}$	44	4.73×10^{-13}
61	$>2.2\times10^{-8}$	61	$>2.2\times10^{-8}$	45	6.48×10^{-13}
62	$>2.2\times10^{-8}$	62	$>2.2\times10^{-8}$	46	9.49×10^{-13}
63	$>2.2\times10^{-8}$	63	$>2.2\times10^{-8}$	47	$>1.20\times10^{-12}$

Table 4c. Digitization levels of signal amplitudes for the lower four decades of charge measurements for the *Ulysses* Dust Detector. For further explanations see Table 4a

IA	Q_I pos. (C)	EA	Q_E neg. (C)	CA	Q_C neg. (C)	PA	Q_P neg. (C)
0	$<9.0\times10^{-15}$	0	$<8.5\times10^{-15}$	0	$<8.8\times10^{-14}$	0	$<1.5\times10^{-14}$
1	1.16×10^{-14}	1	1.16×10^{-14}	1	1.34×10^{-13}	1	2.25×10^{-14}
2	1.73×10^{-14}	2	1.65×10^{-14}	2	2.17×10^{-13}	2	2.93×10^{-14}
3	2.36×10^{-14}	3	2.12×10^{-14}	3	2.78×10^{-13}	3	3.59×10^{-14}
4	3.18×10^{-14}	4	2.77×10^{-14}	4	3.66×10^{-13}	4	4.65×10^{-14}
5	4.46×10^{-14}	5	3.88×10^{-14}	5	4.85×10^{-13}	5	6.81×10^{-14}
6	6.10×10^{-14}	6	5.56×10^{-14}	6	6.47×10^{-13}	6	1.02×10^{-13}
7	9.01×10^{-14}	7	7.95×10^{-14}	7	8.70×10^{-13}	7	1.34×10^{-13}
8	1.30×10^{-13}	8	1.14×10^{-13}	8	1.17×10^{-12}	8	1.65×10^{-13}
9	1.73×10^{-13}	9	1.64×10^{-13}	9	1.62×10^{-12}	9	2.22×10^{-13}
10	2.41×10^{-13}	10	2.32×10^{-13}	10	2.19×10^{-12}	10	3.18×10^{-13}
11	3.23×10^{-13}	11	3.24×10^{-13}	11	3.01×10^{-12}	11	5.44×10^{-13}
12	4.50×10^{-13}	12	4.42×10^{-13}	12	4.22×10^{-12}	12	9.81×10^{-13}
13	6.24×10^{-13}	13	6.05×10^{-13}	13	5.93×10^{-12}	13	9.81×10^{-13}
14	8.54×10^{-13}	14	8.43×10^{-13}	14	8.06×10^{-12}	14	9.81×10^{-13}
15	1.03×10^{-12}	15	1.02×10^{-12}	15	9.76×10^{-12}	15	9.81×10^{-13}
16	1.03×10^{-12}	16	1.02×10^{-12}	16	9.76×10^{-12}	16	9.81×10^{-13}
17	1.03×10^{-12}	17	1.02×10^{-12}	17	1.28×10^{-11}	17	1.30×10^{-12}
18	1.17×10^{-12}	18	1.02×10^{-12}	18	1.81×10^{-11}	18	1.65×10^{-12}
19	2.01×10^{-12}	19	1.58×10^{-12}	19	2.40×10^{-11}	19	2.64×10^{-12}
20	3.61×10^{-12}	20	2.77×10^{-12}	20	3.24×10^{-11}	20	4.06×10^{-12}
21	5.02×10^{-12}	21	3.76×10^{-12}	21	4.33×10^{-11}	21	5.52×10^{-12}
22	6.90×10^{-12}	22	5.16×10^{-12}	22	5.65×10^{-11}	22	7.02×10^{-12}
23	9.60×10^{-12}	23	7.05×10^{-12}	23	7.64×10^{-11}	23	9.46×10^{-12}
24	1.30×10^{-11}	24	9.57×10^{-12}	24	1.06×10^{-10}	24	1.33×10^{-11}
25	1.76×10^{-11}	25	1.31×10^{-11}	25	1.53×10^{-10}	25	1.85×10^{-11}
26	2.48×10^{-11}	26	1.82×10^{-11}	26	2.17×10^{-10}	26	2.70×10^{-11}
27	3.39×10^{-11}	27	2.58×10^{-11}	27	2.99×10^{-10}	27	5.18×10^{-11}
28	4.55×10^{-11}	28	3.65×10^{-11}	28	4.30×10^{-10}	28	1.07×10^{-10}
29	6.16×10^{-11}	29	5.11×10^{-11}	29	6.32×10^{-10}	29	2.39×10^{-10}
30	8.43×10^{-11}	30	6.95×10^{-11}	30	1.15×10^{-9}	30	$>4.0\times10^{-10}$
31	1.04×10^{-10}	31	8.67×10^{-11}	31	$>1.70\times10^{-9}$	31	$>4.0\times10^{-10}$

Table 4d. Digitization steps (IA, EA, PA) of signal amplitudes Q_I, Q_E, Q_P for the two upper decades of Q_I and Q_E and positive charges Q_P—for the *Ulysses* Dust Detector. For further explanations see Table 4a

IA	Q_I pos. (C)	EA	Q_E neg. (C)	PA	Q_P pos. (C)
48	1.04×10^{-10}	48	8.67×10^{-11}	32	$<1.4\times10^{-14}$
49	2.04×10^{-10}	49	2.05×10^{-10}	33	1.56×10^{-14}
50	4.04×10^{-10}	50	4.74×10^{-10}	34	2.06×10^{-14}
51	4.63×10^{-10}	51	5.39×10^{-10}	35	3.06×10^{-14}
52	5.57×10^{-10}	52	6.60×10^{-10}	36	4.29×10^{-14}
53	7.04×10^{-10}	53	8.22×10^{-10}	37	5.99×10^{-14}
54	9.38×10^{-10}	54	1.02×10^{-9}	38	9.00×10^{-14}
55	1.29×10^{-9}	55	1.34×10^{-9}	39	1.25×10^{-13}
56	1.73×10^{-9}	56	1.85×10^{-9}	40	1.69×10^{-13}
57	2.37×10^{-9}	57	2.65×10^{-9}	41	2.31×10^{-13}
58	3.43×10^{-9}	58	4.23×10^{-9}	42	3.18×10^{-13}
59	6.15×10^{-9}	59	7.67×10^{-9}	43	4.37×10^{-13}
60	$>9.00\times10^{-9}$	60	$>1.05\times10^{-8}$	44	8.69×10^{-13}
61	$>9.00\times10^{-9}$	61	$>1.05\times10^{-8}$	45	1.60×10^{-12}
62	$>9.00\times10^{-9}$	62	$>1.05\times10^{-8}$	46	4.35×10^{-12}
63	$>9.00\times10^{-9}$	63	$>1.05\times10^{-8}$	47	$>9.50\times10^{-12}$

Table 5a. Rise-times t_I, t_E, and corresponding speeds v_{t_I}, v_{t_E}, as well as time differences between various signals t_{EI}, t_{PE} for the *Galileo* Dust Detector as a function of digitization step. The indicated times correspond to the logarithmic mean of the lower and upper threshold values of the respective signal amplitude—unless explicit upper and lower limit are given. The rise-times t_I and t_E and the corresponding speeds v_{t_I}, v_{t_E} refer to signal steps IA and EA < 16; for higher signal steps, add 2 to the IT and ET values as discussed in the Impact calibration section

IT	t_I (μs)	v_{t_I} (km s^{-1})	ET	t_E (μs)	v_{t_E} (km s^{-1})	EIT	t_{EI} (μs)	PET	t_{PE} (μs)	PET	t_{PE} (μs)
0	<10.0	70.0	0	<10.0	70.0	0	< −5.0	0	<1.0	16	70.2
1	14.6	70.0	1	14.6	70.0	1	−3.7	1	3.7	17	77.2
2	17.0	70.0	2	17.0	70.0	2	−2.7	2	6.9	18	84.4
3	19.5	70.0	3	19.5	70.0	3	−1.6	3	10.1	19	92.2
4	22.2	70.0	4	22.2	70.0	4	−0.5	4	13.5	20	101
5	25.3	70.0	5	25.3	70.0	5	0.6	5	17.2	21	110
6	28.5	39.6	6	28.5	70.0	6	2.3	6	20.8	22	122
7	32.2	29.8	7	32.2	56.0	7	4.0	7	24.6	23	134
8	36.7	19.0	8	36.7	36.7	8	5.9	8	28.6	24	147
9	41.4	12.7	9	41.4	31.3	9	7.9	9	32.8	25	163
10	46.9	9.7	10	46.9	26.5	10	10.8	10	37.4	26	182
11	53.4	7.2	11	53.4	20.2	11	14.0	11	42.3	27	205
12	61.3	4.5	12	61.6	11.8	12	18.3	12	47.2	28	234
13	71.7	2.3	13	72.5	7.7	13	24.5	13	52.3	29	276
14	88.5	2.0	14	87.8	3.2	14	35.1	14	57.9	30	349
15	>96.0	2.0	15	>97.6	2.3	15	>44.0	15	63.9	31	>404

charge Q_I. It has been recognized by Göller and Grün (1989), however, that this charge ratio depends on impact speed. The following expressions refer only to the low impact speed case ($\sim$5 km s^{-1}). The amplification A is a function of the high voltage HVC [V] applied to the channeltron (which can be commanded in 16 steps HV = 0–15): $A = A_0 \cdot \exp(b \cdot \mathrm{HVC})$, where A_0 is the amplification at a reference voltage (HVC = 1200 V), and b is the sensitivity. Laboratory calibrations have yielded $A_0 \sim 100$ and $b \sim 8 \times 10^{-3}$. In order to compensate for amplification losses during the channeltron lifetime, the high voltage can be varied from 900 (HV = 1) to 2500 V (HV = 15) in steps of approximately 115 V (corresponding to amplification steps of about a factor 2). An additional high voltage step with 200 V (HV = 0) was introduced in order to enable ground tests in ambient conditions.

Either polarity of the induced charge Q_P, when present, can be measured. Logarithmic steps 1–30 cover about four decades of negative charges, while steps 32–47 cover two and nearly three decades of positive charges for *Galileo* and *Ulysses*, respectively (see Tables 4a–d). Since the amplifiers for the charge signal Q_P are rather slow, the induced charge signals at speeds $v > 15$ km s^{-1} are strongly attenuated and cannot be used reliably.

Tables 5a and b show the time measurements (t_I, t_E, t_{EI} and t_{PE}) and the corresponding speed values (v_{t_I} and v_{t_E}) according to impact calibrations for the *Galileo* and *Ulysses* detectors, respectively. Sixteen digitization steps cover about a factor 10 in rise-times t_I and t_E. The coincidence time t_{EI} between signals Q_E and Q_I is used primarily for reliable impact identification. It spans a range from -5 μs (i.e. the ion signal Q_I is detected before the electron signal Q_E) to $+44$ μs. In dust accelerator tests, the negative branch of the t_{EI} range only occurred with highly positively charged dust grains. In case an induced charge Q_P is detected, the flight time t_{PE} through the sensor can also be determined. The time t_{PE} between signals Q_P and Q_E is measured in 32 steps over a range from about 4 to 400 μs. The corresponding distance that the particle travels depends on the details of its trajectory through the sensor. This distance ranges from 9 to 33 cm with a mean distance of 20 cm adopted for flight data reduction.

Impact calibrations

Extensive calibration runs have been performed with dust detectors similar to those aboard *Galileo* and *Ulysses* (Göller and Grün, 1985, 1989) at the Heidelberg dust accelerator. No significant differences between the various individual instruments (engineering, spare or flight models) have been found during impact calibration. Impact calibration tests were performed with iron, carbon, and silicate particles at varying impact angles in the speed range from 2 to 70 km s^{-1} and in the mass range from 10^{-15} to 10^{-10} g. Since the ranges of both speed and mass are very large, logarithmic averaging of several values and logarithmic uncertainties (factors rather than differences) are used in the data reduction.

The signal strength depends moderately on material properties (Kissel and Krueger, 1987) and also on the impact angle. Since neither the chemical composition of the impinging meteoroids nor their impact angles are known, conditions averaged over impact angles and particle composition are assumed. We assume that iron, silicate and carbon represent interplanetary iron-, rock-, and carbonaceous- or CHON- (Kissel *et al.*, 1986) micrometeoroids and take an equal weight average of these three materials. Impact calibrations performed at different impact angles were weighted according to an isotropic influx and then averaged as described below.

The impact speed is obtained from the rise-time measurements t_I and t_E (see Table 5 and Fig. 2). The

Table 5b. Rise-times t_I, t_E, and corresponding speeds v_{t_I}, v_{t_E}, as well as time differences between various signals t_{EI}, t_{PE} for the *Ulysses* Dust Detector. For further explanations see Table 5a

IT	t_I (μs)	v_{t_I} (km s^{-1})	ET	t_E (μs)	v_{t_E} (km s^{-1})	EIT	t_{EI} (μs)	PET	t_{PE} (μs)	PET	t_{PE} (μs)
0	<10.0	70.0	0	<10.0	70.0	0	<−5.0	0	<1.0	16	71.8
1	13.4	70.0	1	13.4	70.0	1	−3.6	1	3.9	17	78.9
2	15.7	70.0	2	15.7	70.0	2	−2.5	2	7.2	18	86.0
3	18.2	70.0	3	18.2	70.0	3	−1.2	3	10.5	19	93.6
4	20.9	70.0	4	20.9	70.0	4	0.0	4	13.6	20	102
5	23.8	70.0	5	23.8	70.0	5	1.2	5	17.4	21	112
6	27.1	43.5	6	27.1	70.0	6	2.8	6	21.1	22	123
7	30.7	34.1	7	30.7	56.0	7	4.7	7	25.0	23	135
8	34.9	21.4	8	34.9	36.7	8	6.8	8	29.2	24	149
9	39.7	14.1	9	39.7	31.3	9	9.2	9	33.5	25	166
10	45.2	10.4	10	45.2	26.5	10	12.1	10	38.1	26	185
11	51.6	7.8	11	51.6	20.2	11	15.6	11	43.3	27	208
12	59.7	5.0	12	59.7	11.8	12	20.1	12	48.4	28	238
13	70.5	2.5	13	70.5	7.7	13	26.4	13	53.3	29	284
14	86.3	2.0	14	86.3	3.2	14	36.9	14	59.0	30	366
15	>96.5	2.0	15	>96.5	2.3	15	>45.0	15	65.2	31	>426

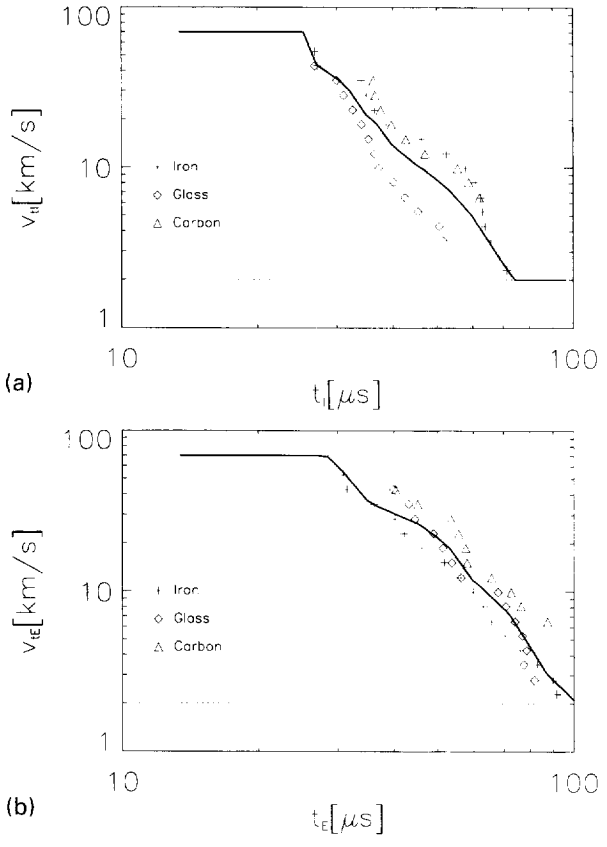

Fig. 2. Calibrations of speed v as functions of ion rise-times t_I and t_E. Results from dust accelerator tests (Göller and Grün, 1989) are shown for different projectile materials. The solid line (average values) shows the actual calibration used in the data reduction. The range of validity (2–70 km s^{-1}) lies between the horizontal dashed lines. (a) Speed v_{t_I} as function of ion rise-time t_I. (b) Speed v_{t_E} as function of electron rise-time t_E

calibration curves used correspond to the mean values obtained for the three different projectile materials with which the instruments were calibrated. A rise-time measurement is started when the respective signal exceeds its threshold and is stopped by a flag pulse from a peak-detector. Impact calibration was performed in the speed interval from about 2 to 70 km s^{-1}, so impact speeds derived from rise-time measurements will also be limited to this range. Dust accelerator tests as well as experience with flight data have shown that (1) the shape of the ion signal is less susceptible to noise than the shape of the electron signal and (2) the electron amplitude values EA are generally 2–6 times larger than the ion amplitude values IA for true impacts. As a consequence, the electron rise-time is only used for the impact speed determination if $2 \leqslant \text{EA-IA} \leqslant 6$. Since both speed measurements, if available, are independent, one obtains two (often different) values v_{t_I} and v_{t_E}. We take the impact speed v to be the geometric mean of both speeds $v = \sqrt{(v_{t_I} \cdot v_{t_E})}$. The minimum error in v of 1.6 is achieved if both individual speeds agree within a factor of 2. If the ratio of both individual speeds exceeds 2, then the uncertainty can increase to about 10 in the calibrated speed range. If only one speed is measured, then the minimum uncertainty is VEF = 2. Upper and lower speeds are obtained by multiplying and dividing the mean speed v by these uncertainty factors ($v_{up} = v \cdot \text{VEF}$ and $v_{lo} = v/\text{VEF}$). If a signal is either just above the threshold or near saturation, then the rise-time values are indeterminate and no speed value can be derived. In these cases, both the speed v and the uncertainty factor are set to 11.8. In any case, a speed value with an uncertainty factor VEF > 6 (i.e. $v_{up}/v_{lo} > 36$) should be ignored.

The rise-times t_I and t_E and the corresponding speed values v_{t_I} and v_{t_E} are shown in Fig. 2 (cf. Table 5). Table 5 refers to small signals for which IA < 16 and EA < 16. It has been found in laboratory calibrations and statistically verified in data from the space instruments that the rise-times t_I and t_E of big signals processed by the upper amplifier chains (represented by IA > 16 and EA > 16) are systematically short. Therefore, the rise-times t_I and t_E and the resulting impact speed values, v_{t_I} and v_{t_E}, are corrected by adding 2 to the IT and ET values measured with higher signal levels.

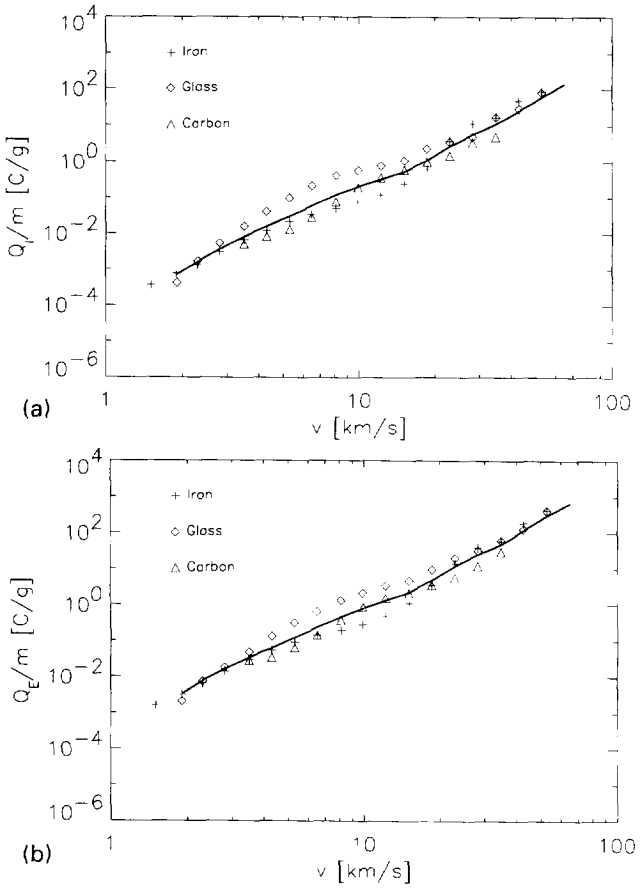

Fig. 3. Calibration of impact charge over mass ratio Q/m as a function of impact speed v for three different materials (Göller and Grün, 1989). The solid line shows the actual calibration used in the data reduction. (a) Impact charge Q_I/m vs. speed. (b) Impact charge Q_E/m vs. speed

The coincidence time t_{EI} (as determined by the EIT value and the EIC coincidence) is an important indicator used to separate impacts from noise signals. Baguhl *et al.* (1993) found that most impacts have t_{EI} values ranging from 0.2 to 45 μs. Events where the fast coincidence (EIC) between Q_E and Q_I is set ($t_{EI} < 0.2$ μs) are found to be primarily noise events. If the channeltron signal Q_C exceeds its threshold, the coincidence (ICC) between Q_I and Q_C is also a reliable indicator for true impacts.

Once the particle's speed has been determined, Q_I/m and Q_E/m can be found from the calibration curves given in Figs 3a and b. From these values and the respective impact charges, two independent estimates of the mass can be derived. The measured mass is then taken to be the geometric mean of these two values (i.e. $m = \sqrt{(m_{Q_I} \cdot m_{Q_E})}$). If the speed is well determined (VEF = 1.6) then the mass value can be determined with an uncertainty factor MEF = 6. Larger speed uncertainties can result in mass uncertainty factors greater than 100. Upper (m_{up}) and lower (m_{lo}) mass values are obtained by multiplying and dividing the mean mass m by the mass uncertainty factor MEF. If the speed value is discarded, then the mass value must be discarded too.

The induced charge signal Q_P is a measure of the electric charge carried by a dust particle entering the dust sensor. This induced charge depends moderately on the actual position of the dust particle as it flies through the charge grid. Tests in the laboratory with a large number of charged dust particles showed that on average the induced charge is only a fraction of the dust charge, typically $55 \pm 10\%$. A dust grain will induce only part of its charge on the charge sensing grid because of the proximity of the charge sensing grid to the other grounded grids (15 mm).

The induced charge measurement is the most difficult measurement of the *Galileo* and *Ulysses* Dust Detectors for two reasons:

(1) Dust particles in space are only weakly charged by photoelectrons or low-energy plasma electrons. A surface potential U results in a dust charge $q = 4\pi\varepsilon_0 Us$ for a spherical particle of radius s and with permittivity $\varepsilon_0 = 8.859 \times 10^{-12}$ C V^{-1} m^{-1}. At a typical surface potential of $U = 5$ V, the smallest particle exceeding the detection threshold has a radius of about 50 μm or a corresponding mass of 6×10^{-7} g at an assumed density of 1 g cm^{-3}. Most of the particles detected so far are several orders of magnitude smaller than this.

(2) The charge grid is the measuring channel most exposed to ambient noise from both internal and exterior causes. Noise signals a factor of ten above the threshold are quite common on this channel and so analysis of this measurement channel requires careful consideration of the noise environment at the time of a dust impact. As a consequence, the times t_{PE} between the entrance grid signal (Q_P) and the target impact signal (Q_E) have not yet been determined.

Onboard data processing

In this section, we describe the data processing which occurs on board the spacecraft and in the next, that which is done on the ground. First, the instrument microprocessor, which controls the experiment measurement cycle, collects the buffered data and processes the data according to its onboard program. This takes about 5 ms (10 ms for *Galileo* after reprogramming in June 1990). The information on a single event (dust impact or noise) is contained in an Experiment Data Frame (EDF) of 16 bytes (i.e. 128 bits).

The impact times are recorded with an accuracy of 4 h for most of the *Galileo* mission (this value has been set in order to bridge gaps in the data transmission as long as one month) and with an accuracy of 2 s in the case of *Ulysses*. In both cases, the rotation angle at the time of impact is recorded so directional information is not lost. The sensor pointing at the time of impact is described by the angle through which the spacecraft has rotated, about its spin axis. This "spin angle" is described by the SEC word. The positive direction of spin axis pointing and the zero reference angle definitions for the *Galileo* and *Ulysses* spacecraft differ from each other and will be described in more detail below (see also Paper II).

The instruments are designed to reliably operate under noisy conditions thereby allowing the extraction of true dust impacts from noise events. True impacts can be detected at rates of as low as one per month. This is achieved by raising the threshold levels of all impact sig-

Table 6a. Thresholds of the various charge measurement channels as function of threshold settings (ICP, ECP, CCP, PCP)—for the *Galileo* Dust Detector

ICP	Q_I pos. (C)	ECP	Q_I neg. (C)	CCP	Q_C neg. (C)	PCP	Q_P pos. (C)	Q_P neg. (C)
0	1.0×10^{-14}	0	9.8×10^{-15}	0	1.0×10^{-13}	0	9.2×10^{-15}	1.8×10^{-14}
1	2.6×10^{-14}	1	2.4×10^{-14}	1	2.4×10^{-13}	1	2.3×10^{-14}	3.8×10^{-14}
2	5.8×10^{-14}	2	5.5×10^{-14}	2	5.2×10^{-13}	2	5.0×10^{-14}	7.3×10^{-14}
3	1.5×10^{-13}	3	1.4×10^{-13}	3	1.2×10^{-12}	3	1.2×10^{-13}	1.5×10^{-13}

Table 6b. Thresholds of the various charge measurement channels as function of threshold settings (ICP, ECP, CCP, PCP)—for the *Ulysses* Dust Detector

ICP	Q_I pos. (C)	ECP	Q_I neg. (C)	CCP	Q_C neg. (C)	PCP	Q_P pos. (C)	Q_P neg. (C)
0	9.0×10^{-15}	0	8.5×10^{-15}	0	8.8×10^{-14}	0	1.4×10^{-14}	1.5×10^{-14}
1	2.7×10^{-14}	1	2.6×10^{-14}	1	2.6×10^{-13}	1	4.3×10^{-14}	4.4×10^{-14}
2	6.3×10^{-14}	2	6.0×10^{-14}	2	5.8×10^{-13}	2	1.0×10^{-13}	1.0×10^{-13}
3	1.6×10^{-13}	3	1.5×10^{-13}	3	1.5×10^{-12}	3	2.6×10^{-13}	2.5×10^{-13}

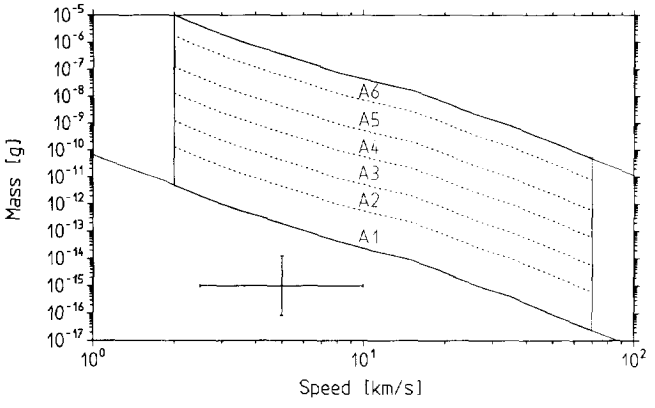

Fig. 4. Calibrated mass and speed ranges m vs. v of the *Galileo* and *Ulysses* Dust Detectors. The tilted boxes show the six amplitude ranges AR = 1–6. No impacts can be detected below AR = 1; above AR = 6, signals are saturated yielding only lower mass and speed limits. Below 2 km s^{-1} and above 70 km s^{-1}, speeds and masses are undetermined. The bottom cross represents typical accuracies of mass and speed values

nals individually (cf. Table 6) by telecommand which allows us to adapt the instrument sensitivity to the actual noise environment on board the spacecraft. Coincidences between the signals are established which, along with the signal amplitudes, are used to classify each event.

Each measured event (noise or impact) is classified according to the strength of its ion signal (IA) into one of six amplitude ranges (AR = 1–6). Each amplitude range corresponds roughly to one decade in electronic charge Q_I. The correspondence between these amplitude ranges and a particle's mass and velocity for both the *Galileo* and *Ulysses* Dust Detectors is shown in Fig. 4. In addition, each event is categorized into one of four event classes (described by the class number CLN). The event classification scheme, which defines criteria that must be satisfied for each class, is shown in Table 7. Within each class these conditions are connected by logical "and" except where noted. Class 0 (CLN = 0) includes all events that are not categorized in a higher class (typically noise and unusual impact events—e.g. impacts onto the sensor's internal structure other than the impact target). In classes 1–3, the criteria become increasingly restricted so that CLN = 3 generally represents true dust impact events only. Some of the set point values (SP01–SP15), which can be set by ground command, are used in the classification scheme. Four classes, together with six amplitude ranges, constitute 24 separate categories. Each of these categories has its own 8-bit accumulator (AC, see Table 8a). As long as the respective accumulator does not overflow, each event is counted even if the complete information is not received on ground. Generally, the event rate is so low (even in the low amplitude and low class ranges) that the true increment can be reliably determined. Flight experience has shown that all categories and corresponding accumulators—excluding AC01, AC11 and AC02—contain primarily impact events. Even in these latter categories, true impacts can be identified and separated from noise events if the complete data set for an event is available (Baguhl *et al.*, 1993).

The onboard data processing supports the application of a priority scheme for the data transmission. Data from events with different categories are stored in different ranges of the onboard memory. The organization of the memory is particularly important for *Galileo* because of its severely limited transmission rate. Data must be safely stored on board for long periods of time. Here we describe the memory setup and how it helps us to recover complete information about true dust impacts on the ground.

The memory is divided into separate ranges in which various data is given priority. The A range of instrument memory stores the six most recent EDFs—one for each amplitude range regardless of class. The E range, graphically depicted in Table 8b, stores the last 8 (for *Galileo* the last 16 after reprogramming in June 1990) events occurring within class 3. These events satisfy the most stringent constraints and are almost certainly true impacts. Additional memory ranges F, G, and H (see

Table 7. Onboard classification scheme. Set points have the following values: SP01 = 1, SP02 = 15, SP03 = 1, SP04 = 15, SP09 = 2, SP10 = 8, SP11 = 8, SP14 = 0, SP15 = 0, SP16 = 0. Missing set points are not used in this classification scheme

Parameters	CLN = 0	CLN = 1	CLN = 2	CLN = 3
iongrid amplitude (IA)	IA > 0 or	(IA > 0 or	IA > 0	IA > SP16
target amplitude (EA)	EA > 0 or	EA > 0)	EA > 0	EA > SP14
channeltron amplitude (CA)	CA > 0	CA > 0	CA > 0	CA > SP15
EA rise-time (ET)			SP03 ⩽ ET ⩽ SP04	SP03 ⩽ ET ⩽ SP04
IA rise-time (IT)			SP01 ⩽ IT ⩽ SP02	SP01 ⩽ IT ⩽ SP02
target–iongrid coincidence (EIC)			EIC = 0	EIC = 0
channeltron–iongrid coincidence (ICC)			ICC = 1	ICC = 1
noise counter of:				
target (EN)				EN ⩽ SP11
iongrid (IN)				IN ⩽ SP09
channeltron (CN)				CN ⩽ SP10

Table 8a. Event classification scheme and accumulator (AC) matrix

IA	Amplitude range	Class number (CLN) 0	1	2	3
0–7	AR = 1	AC01	AC11	AC21	AC31
8–15	AR = 2	AC02	AC12	AC22	AC32
16–23	AR = 3	AC03	AC13	AC23	AC33
24–32	AR = 4	AC04	AC14	AC24	AC34
48–55	AR = 5	AC05	AC15	AC25	AC35
56–63	AR = 6	AC06	AC16	AC26	AC36

Table 8b. Memory allocation (E, F, G, and H ranges)

IA	Amplitude range	Class number (CLN) 0	1	2	3
0–7	AR = 1	H	G	G	E
8–15	AR = 2	F	F	F	E
16–23	AR = 3	F	F	F	E
24–32	AR = 4	F	F	F	E
48–55	AR = 5	F	F	F	E
56–63	AR = 6	F	F	F	E

Table 8b) were added to the *Galileo* memory scheme during reprogramming. The last 8 EDFs in each of these ranges are also stored.

The transmission of seven EDFs constitutes an instrument read-out cycle which is continuously repeated. It comprises the six A-range events and one of the E-range events (in case of *Galileo* after reprogramming one of the E, F, G, and H ranges). The E, F, G, and H ranges are cyclically permuted so that successive read-out cycles cover the full range of instrument memory. The additional memory for *Galileo* helps to offset losses that occur because of infrequent memory read outs.

The onboard classification (Table 7) can be adapted to the in-flight noise environment by changing the thresholds and classification parameters (set points) or by adjusting the onboard classification program through telecommands. Detailed information on noise is mandatory in order to evaluate the reliability of impact detection for the various event categories, to minimize the effect on dead-time and to optimize memory utilization.

Data processing on the ground

After receiving the partially processed data from the spacecraft, the following data processing steps are performed on the ground:

(1) instrument health check,
(2) generation of accumulator histories,
(3) extraction of discrete events,
(4) reduction of impact data,
(5) generation of data products.

The instrument health check involves inspection of instrument house keeping data such as temperatures, voltages, currents and a check of the test pulse data. If, for example, the temperature readings are too high, the heater power level can be set accordingly. Once per day (during encounter times more frequently) all 24 accumulators are checked and history plots covering appropriate time intervals for impact and noise events are produced. If excessive noise is detected then appropriate measures, such as changing the thresholds or channeltron high voltage by telecommand, can be taken. Occasionally, tests of different instrument modes are performed in order to probe the actual noise environment; the instrument parameters can then be adjusted accordingly.

Step 3, the extraction of discrete event data, includes the removal of redundant information, which can occur because of the design of the instrument's memory, and a completeness check during which all events that have caused an increment of one of the 24 accumulators are searched for. Data of these events are put in time order. The next step is the identification and reduction of impact data as described in the "Impact calibration" section. Supplementary data, including spacecraft position and spin axis pointing, are added to each impact record. These supplementary data are derived from project specific data sources (SPICE routines and files for *Galileo* and SEDR files for *Ulysses*). The instrument pointing direction at the time of impact is commonly defined by both the pointing direction of the spacecraft spin axis and the rotation angle, which varies uniformly from 0° to 360° during one spin revolution.

For *Ulysses*, the positive direction of the spacecraft spin axis (aligned with the high gain antenna) points from the

spacecraft roughly toward Earth. For *Galileo*, however, the positive spin axis points approximately antisunward over most of the spacecraft trajectory. Spin angle reference "zero" is separately defined by onboard Sun or star tracker sensors for the two spacecraft. However, we find it convenient for purposes of analyzing dust impact data to re-define "zero" rotation angle to occur when the dust sensor axis passes closest to ecliptic north during spacecraft rotation. For consistency, increasing rotation angle has been defined to follow the spin of the *Ulysses* spacecraft and to be opposite to the spin of the *Galileo* spacecraft. Thus for both spacecraft, rotation angle ROT = 90 is roughly the direction in which circular prograde particles move (see Paper II).

The preparation of data products is the final routine step of dust data processing. A number of separate files are produced which reflect various stages of data processing. The most important are the accumulator data file ADF and the dust parameter file DPF. The ADF contains accumulator data, time and orbit information at a resolution of 24 h during cruise and 30 min during planetary encounters. The DPF contains fully reduced impact data together with supplementary information. We are currently depositing equivalent data in public archives such as Planetary Data System, NSSDC and the ESA *Ulysses* Data Center.

References

Auer, S. and Sitte, K., Detection technique for micrometeoroids, using impact ionization. *Earth Planet. Sci. Lett.* **4**, 178–183, 1968.

Baguhl, M., Grün, E., Linkert, D., Linkert, G. and Siddique, N., Identification of "small" dust impacts in the *Ulysses* dust detector data. *Planet. Space Sci.* **41**, 1079–1092, 1993.

Dalmann, B. K., Grün, E. and Kissel, J., The ion composition of the plasma produced by impact of fast particles. *Planet. Space Sci.* **25**, 135–147, 1976.

Dietzel, H., Eichhorn, G., Fechtig, H., Grün, E., Hoffman, H.-J. and Kissel, J., The HEOS 2 and Helios micrometeoroid experiments. *J. Phys. (E) Scient. Instrum.* **6**, 209–217, 1973.

Fechtig, H., Grün, E. and Kissel, J., Laboratory simulation, in *Cosmic Dust* (edited by J. A. M. McDonnell), pp. 607–669. Wiley, Chichester, 1978.

Friichtenicht, J. F. and Slattery, J. C., Ionization associated with hypervelocity impact. NASA Technical Note D-2091, 1963.

Göller, J. R. and Grün, E., Calibration of the Galileo/ISPM dust detectors with iron particles, in *Properties and Interactions of Interplanetary Dust* (edited by R. H. Giese and P. Lamy), pp. 113–115. D. Reidel, Dordrecht, 1985.

Göller, J. R. and Grün, E., Calibration of the *Galileo/Ulysses* dust detectors with different projectile materials and at varying impact angles. *Planet. Space Sci.* **37**, 1197–1202, 1989.

Göller, J. R., Grün, E. and Maas, D., Simulation of particle impacts on an ionization detector (DIDSY IPM-P). ESA SP 250, Vol. III, pp. 333–336, 1986.

Grün, E., Impact ionization from gold, aluminium and PCB-Z, in *The Giotto Spacecraft Impact-induced Plasma Environment*, ESA SP 224, pp. 39–41, 1984.

Grün, E., Berg, O. E. and Dohnany, J., Reliability of cosmic dust data from Pioneers 8 and 9, in *Space Research XIII* (edited by M. J. Rycroft and S. K. Runcorn), pp. 1057–1062. Akademieverlag, Berlin, 1973.

Grün, E., Fechtig, H., Giese, R. H., Kissel, J., Linkert, D., Maas, D., McDonnell, J. A. M., Morfill, G. E., Schwehm, G. and Zook, H. A., The Ulysses dust experiment. *Astron. Astrophys. Suppl. Ser.* **92**, 411–423, 1992a.

Grün, E., Fechtig, H., Hanner, M. S., Kissel, J., Lindblad, B.-A., Linkert, D., Linkert, G., Morfill, G. E. and Zook, H. A., The Galileo Dust Detector. *Space Sci. Rev.* **60**, 317–340, 1992b.

Grün, E., Baguhl, M., Divine, N., Fechtig, H., Hamilton, D. P., Hanner, M. S., Kissel, J., Lindblad, B.-A., Linkert, D., Linkert, G., Mann, I., McDonnell, J. A. M., Morfill, G. E., Polanskey, C., Riemann, R., Schwehm, G., Siddique, N., Staubach, P. and Zook, H. A., Three years of *Galileo* dust data. *Planet. Space Sci.* **43**, 953–969, 1995a.

Grün, E., Baguhl, M., Divine, N., Fechtig, H., Hamilton, D. P., Hanner, M. S., Kissel, J., Lindblad, B.-A., Linkert, D., Linkert, G., Mann, I., McDonnell, J. A. M., Morfill, G. E., Polanskey, C., Riemann, R., Schwehm, G., Siddique, N., Staubach, P. and Zook, H. A., Two years of *Ulysses* dust data. *Planet. Space Sci.* **43**, 971–999, 1995b.

Iglseder, H. and Igenbergs, E., Measured charge generation by small mass impact at velocities between 1 and 45 km/s. *Int. J. Impact Engng* **5**, 381–388, 1987.

Kissel, J., The GIOTTO Particulate Impact Analyzer, ESA SP 1077, pp. 67–83, 1986.

Kissel, J. and Krueger, F. R., Ion formation by impact of fast dust particles and comparison with related techniques. *Appl. Phys.* **A42**, 69–85, 1987.

Kissel, J., Sagdeev, R. Z., Bertaux, J. L., Angarov, V. N., Audouze, J., Blamont, J. E., Büchler, H., von Hoerner, H., Inogamov, N. A., Khromov, V. N., Knabe, W., Krueger, F. R., Langevin, Y., Levasseur-Regourd, A. C., Managadze, G. G., Podkolzin, S. N., Sharipo, V. d., Tabaldyev, S. R. and Zubkov, B. V., Compositions of comet Halley dust particles from Vega observations. *Nature* **321**, 336–337, 1986.

Raizer, Yu. P., Residual ionization of a gas expanding in vacuum. *Sov. Phys. JETP* **10**, 411–412, 1960.

Timmermann, R. and Grün, E., Plasma emission from high velocity impacts of microparticles onto water ice, in *Origin and Evolution of Interplanetary Dust* (edited by A. C. Levasseur-Regourd and H. Hasegawa), pp. 375–378. Kluwer, Dordrecht, 1991.